Role of integrin adhesions in cellular mechanotransduction

Balcıoğlu, H.E.

Chapter 4

Substrate rigidity modulates the association between traction forces and molecular composition of cell-matrix adhesions [1]

[1] This chapter is based on: Hayri E Balcıoğlu*, Rolf Harkes*, Thomas Schmidt#, Erik HJ Danen#, Substrate rigidity modulates the association between traction forces and molecular composition of cell matrix adhesions *In Preparation; *:These authors contributed equally to this work. #Shared corresponding authors.*

Abstract

In cell matrix adhesions, integrin receptors and associated proteins provide a dynamic coupling of the extracellular matrix (ECM) to the cytoskeleton. This allows bidirectional transmission of forces between the ECM and the cytoskeleton, which tunes intracellular signaling cascades that control survival, proliferation, differentiation, and motility. The quantitative relationships between recruitment of distinct cell matrix adhesion proteins and local cellular traction forces are not known. Here, we applied dSTORM to cell matrix adhesions formed on fibronectin-stamped PDMS pillars and developed a mathematical approach to relate the number of talin, vinculin, paxillin, and focal adhesion kinase (FAK) molecules to local cellular traction force. We find that FAK recruitment does not show an association with traction force application whereas a ∼60 pN force increase is associated with the recruitment of one talin, two vinculin, and two paxillin molecules on a substrate with an effective stiffness of 47 kPa. On a substrate with a four-fold lower stiffness the stoichiometry of talin:vinculin:paxillin changes from 1:2:2 to 2:12:6 for the same ∼60 pN traction force. The marked relative change in force-related vinculin recruitment indicates a stiffness-dependent switch in vinculin function in cell matrix adhesions. Taken together, application of a novel mathematical approach to super resolution microscopy data reveals substrate stiffness-dependent modulation of the relation between traction force and molecular composition of cell matrix adhesions.

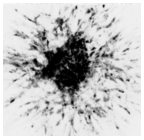

4.1 Introduction

Cell matrix adhesions couple the intracellular cytoskeletal network to the extracellular matrix (ECM) and are key sites for bidirectional mechanotransduction. First, they are the sites where cells apply myosin-driven contractile forces to their environment, for instance during cell migration or tissue remodeling [1]. Second, they allow cells to sense and respond to changes in stiffness of their environment, which is an important mechanical cue regulating stem cell differentiation, cancer progression, and other processes [2, 3].

Cell matrix adhesions contain integrin transmembrane receptors that bind ECM components with their globular head domains, and connect to a large complex of associated proteins with their intracellular tail domains. Integrins and integrin-associated proteins in cell matrix adhesions have been demonstrated to change conformation and/or expose new protein-binding sites when stretched by force [4]. Several of the associated proteins, including talin and vinculin connect the integrin cytoplasmic tails to the F-actin network [5]. Others, such as paxillin and focal adhesion kinase (FAK) are involved in local signaling platforms that regulate actin cytoskeletal dynamics for instance through Rho GTPases [6]. This allows cell matrix adhesions to adjust their molecular architecture in response to force, thereby ensuring a balance between extracellular (ECM) and intracellular (cytoskeletal) forces.

Cell matrix adhesions are highly dynamic structures [7]. Super resolution microscopy techniques have been applied to reveal the 3D multimolecular architecture of cell matrix adhesions [8, 9]. It is well known that larger cell matrix adhesions support higher forces [10–12] but quantitative relationships between recruitment of individual cell matrix adhesion proteins and local traction force application have not been reported. Here, we developed a novel mathematical method for the analysis of antibody-mediated direct stochastic optical reconstruction microscopy (dSTORM) [13] images. For transformation of dSTORM data into molecular counts, we made use of a real space approach, which has similarities to the Fourier ring-correction analysis method [14] and relies on high positional accuracy characteristic of super-resolution imaging. We applied this method to four distinct cell matrix adhesion components, talin, vinculin, paxillin, and FAK, and combined dSTORM with traction force microscopy to determine quantitative relationships between their recruitment to cell matrix adhesions and local traction forces.

For cells plated on a substrate with an effective Young's modulus of 47.2 kPa, we determine that each additional talin, vinculin, and paxillin molecule is accompanied by a 66, 30, and 32 pN increase in traction force, respectively. On an 11.6 kPa substrate the stoichiometry for talin:vinculin:paxillin changes from ∼1:2:2 per ∼60 nN force increment to ∼2:12:6 for the same amount of traction force. Instead, FAK recruitment does not significantly correlate with traction force increases, irrespective of substrate rigidity. These findings provide a first quantitative relationship between recruitment of distinct cell matrix adhesion proteins and local traction forces and reveals remarkable regulation of this relationship by substrate stiffness.

4.2 Results

4.2.1 dSTORM on cell matrix adhesion proteins

We used vinculin knockout MEFs transiently expressing GFP-vinculin to compare signals derived from an Alexa-532-conjugated GFP nanobody to those from a vinculin monoclonal antibody and an Alexa-647-conjugated secondary antibody. Confocal microscopy confirmed that Alexa-532 and Alexa-647 signals co-localized only in GFP positive cell matrix adhesions as expected (Figure 4.1A, top, red arrows; i,ii). As a control, cell matrix adhesions in vinculin null MEFs lacking GFP-vinculin were readily identified using a paxillin antibody (Figure 4.1A, bottom, green arrows; iii) while such adhesions did not stain when the vinculin antibody was used (Figure 4.1A, top).

Next, stainings of Alexa-532-conjugated GFP nanobody and vinculin monoclonal antibody followed by Alexa-647-conjugated secondary antibody in vinculin null/GFP-vinculin cells were processed for dSTORM. dSTORM images showed overlap between Alexa-532 and Alexa-647 localizations (Figure 4.1B). Indeed localizations obtained from the two different fluorophores across 105 adhesions in 11 different cells as determined by dSTORM showed a strong linear dependence (Figure 4.1C).

4.2.2 Combination of dSTORM and cellular traction force measurements

Talin staining followed by confocal imaging identified cell matrix adhesions coupled to fibronectin-stamped µpillars (Figure S1A). The average

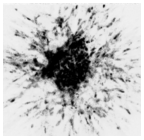

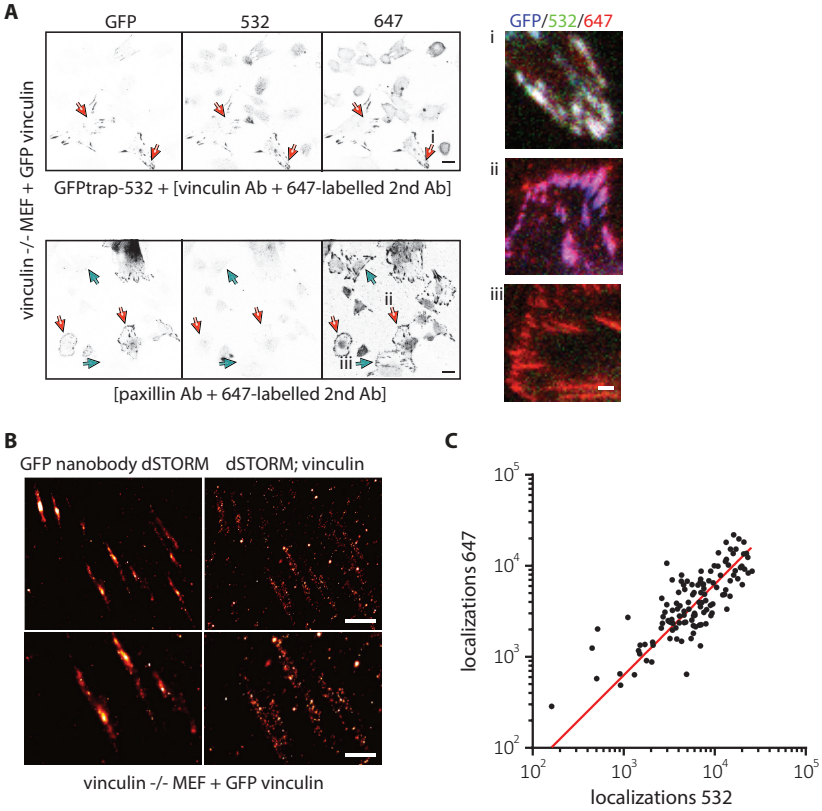

Figure 4.1

dSTORM on cell matrix adhesions. *A, confocal images of vinculin -/- MEFs transiently expressing GFP vinculin, immunostained with the indicated antibodies. Red arrows indicate cells that are GFP (and vinculin) positive, green arrows indicate cells that are GFP (and vinculin) negative. In i, ii and iii merged images for zoom-ins of the indicated adhesions are shown. B, representative dSTORM images of cells immunostained with GFP nanobody conjugated with Alexa 532 obtained with 532 nm laser (left) and [vinculin antibody plus secondary antibody conjugated with Alexa 647] obtained with 647 nm laser (right). C, comparison of number of localizations obtained from individual adhesions by applying dSTORM to first Alexa647 and then to Alexa532. Red line indicates the linear fit (R^2=0.47). Scale bars are 20 µm (A, left panels), 3 µm (A, right panels i-iii), 100 nm (B, top) and 50 nm (B, bottom).*

background deflection, corresponding to the displacement resolution, was 47±23 nm as determined by epi-fluorescence imaging in a cell free region in the field of view of dSTORM imaging (Figure S1B,C). For µpillar arrays with effective Young's moduli of 11.6 kPa or 47.2 kPa (spring constants of 16 nN/µm or 66 nN/µm, respectively), the displacement resolution of ∼50 nm corresponded to a force precision of 0.8 nN and 3 nN, respectively. Combining epi-fluorescence (displacements) and dSTORM, provided visualization of traction force and localizations in cell matrix adhesions (Figure 4.2A).

We established that forces measured in samples fixed for dSTORM application were slightly lower than forces measured by live confocal imaging of pillar deflections in mcherry-lifeact-labelled NIH3T3 cells (Figure 4.2B,C). Nevertheless, the increase in force, induced by seeding cells on a substrate with higher effective Young's modulus as measured post-fixation completely recapitulated the increase measured in live cells, as established previously for fixation for standard immunofluorescence [15]. In accordance with the results obtained by confocal imaging, forces determined by epi-fluorescence microscopy in combination with dSTORM imaging of NIH3T3 cells immunostained for talin showed a ∼3-fold increase for cells seeded on 47.2 kPa as compared to forces applied by cells seeded on 11.6 kPa (Figure 4.2B-D).

4.2.3 From dSTORM localizations to molecule counts

Following dSTORM on µpillar arrays, 2D Gaussian intensity profiles were obtained with an average of 521±404 photons, providing a localization precision of 14±5 nm (Figure 4.3A,B). To estimate the number of talin molecules in an adhesion coupled to one pillar (Figure 4.2B, red box; Figure 4.3C,D), we developed a method that uses the inherent high localization precision in super-resolution microscopy. We based our methodology on analysis of the inter-localization distance distribution in the images, which in turn was used to distinguish between spatially correlated and uncorrelated localizations. This method makes use of the fact that statistics associated with fluorescence labeling and photophysics, although partly unknown, are equivalent for the spatially correlated and uncorrelated localizations.

First, we determined statistics for the cumulative distribution function (cdf) of inter-localization distances within the adhesion shown in Figure 4.3D. For each distance "r" between 2 localizations, the number

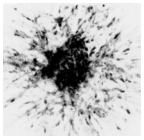

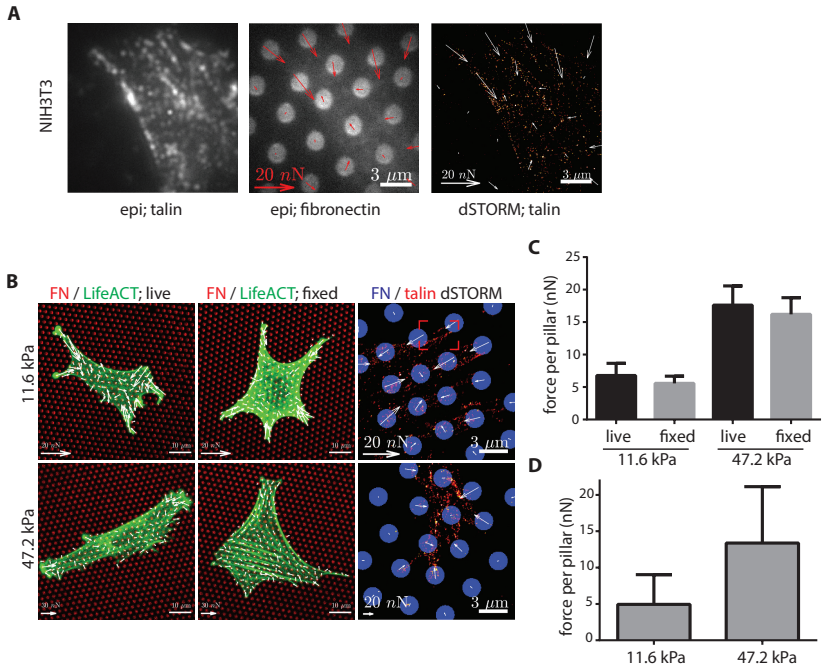

Figure 4.2

Combination of dSTORM with micropillars. *A, NIH3T3 cell imaged with the dSTORM setup using epi-fluorescence with 647 (left) and 405 (middle) or dSTORM with 647 channel (right) together with accompanying force measurements (arrows in middle and right image). B, images of live (left) and fixed (middle and right) NIH3T3 cells on pillars of effective Young's modulus of 11.6 kPa (top) or 47.2 kPa (bottom) stamped with fibronectin conjugated to Alexa647 (left and middle) or to Alexa405 (right). mCherry-LifeACT (left and middle) or talin immunostaining (secondary antibody conjugated with Alexa647) was imaged using confocal imaging (left and middle) or dSTORM setup (right) with calculated forces (arrows). C,D, bar graphs showing mean ± standard deviation of cellular forces applied per pillar calculated from confocal images (C) or images obtained with dSTORM setup (D) for cells on pillars with indicated stiffnesses. Scale bars are 3 µm (A, B-right), 10 µm (B, left and middle); deflection arrow scales are 20 nN (A, B, top-right and bottom) and 30 nN (B, top-left and top-middle).*

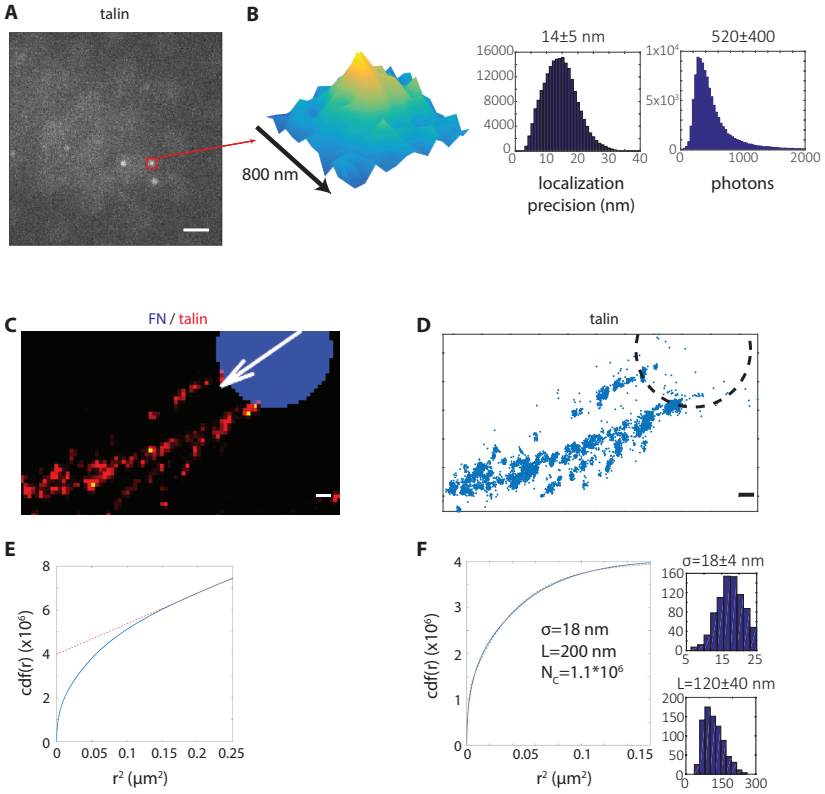

Figure 4.3

Distribution analysis of talin dSTORM localizations in a single adhesion. *A, example image frame from dSTORM acquisition with several Alexa647 molecules fluorescing. B, zoom in of the red square in A (left) and histograms showing the positional accuracy of localizations from this dSTORM acquisition (left) and for the intensity of localizations (right). C, zoom in of the red square from Figure 4.2B. D, image derived from C showing 6700 localizations of Alexa647 targeted to talin associated with one pillar (dashed circle). E, cumulative distance function (cdf) of interlocalization distances from the localizations in D with a linear line fit (red dashed line) from 0.16 µm² to 0.25 µm². F, cdf from E, with linear fit subtracted and accompanying double exponential fit* $cdf(r) = N_c(1-e^{-r^2/4\sigma^2})+N_L(1-e^{-r^2/L^2})$ *with* σ*=18 nm, L=200 nm,* N_c*=1.10x10⁶ and* N_L*=2.9x10⁶. Histograms of fit parameters* σ *(right-top) and L (right-bottom) obtained across all experiments are shown. Scale bars are 2 µm (A) and 250 nm (C, D).*

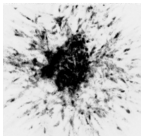

of distances smaller than r as a function of r^2 was obtained. For a spatial random distribution this function would exhibit linear dependence on r^2 since the distances are uncorrelated. However, the relationship between the cdf of inter-localization distances and r^2 showed a two-regime function. A linear regime was observed for high values of r^2, reflecting localizations belonging to different talin molecules (Figure 4.3E). When this linear relationship was subtracted from the distribution, a non-linear regime remained for lower r^2 values (Figure 4.3F). This reflected correlated detections belonging to a single talin molecule or a cluster of talin molecules. A good fit to this non-linear regime was obtained with a double exponential:

$$cdf(r)=N_c\ (1\text{-}e^{-r^2/4\sigma^2})\ +N_L\ (1\text{-}e^{-r^2/L^2})\ .$$

Here r denotes the distance between fluorophores, σ denotes the distribution of detections from a single talin molecule and N_c is the corresponding number of correlated distances. In the second part of the exponential, L is the structure parameter, and N_L is the contribution of spatial structures in the data, i.e. talin molecules in close proximity. The structural length scale, L (120±40 nm), was significantly larger than the positional accuracy, σ(18±4 nm), indicating the two components of the exponential fit to be well separable. From these fits the number of talin molecules in the adhesion (Figure 4.3D) was calculated with the equation $N_m=N^2/(N+N_c)$ (See Materials and methods); where N_m denotes the number of talin molecules and N is the number of detections. Simulations indicated good agreement between the estimated number of molecules and the input: the accuracy was >10% even at high overlap conditions (Figure S1D-F). Using this method, 40 talin molecules were detected in the adhesion shown (Figure 4.3C,D).

4.2.4 Relating the abundance of cell matrix adhesion proteins to traction forces

Next, we generated dSTORM-based localization maps for four different cell matrix adhesion proteins in cells seeded on pillars of two different effective Young's moduli. Cell matrix adhesion areas were selected and corresponding talin, vinculin, paxillin, and FAK molecules were calculated (see Figure S2 for histograms for all measurements and calculations). In order to relate force application to abundance of adhesion molecules, we examined the cross correlation between the determined number of molecules in an adhesion and the measured local traction force. We

then approximated the force induced by recruitment of a single molecule assuming a linear relationship. In >100 cell matrix adhesions from 30 NIH3T3 cells analyzed in 3 independent experiments on µpillars with an effective Young's modulus of 47.2 kPa, the force corresponding to the adhesion showed a strong correlation to the number of talin molecules in the adhesion (Figure 4.4A, Figure S3). This was accompanied by an increase in cell matrix adhesion area (Figure S3). Highly similar talin-force relations were identified across the different experiments. Likewise, experiments performed on µpillar arrays with lower effective Young's modulus (11.6 kPa) provided linear talin-force relations that were similar across different experiments but here, forces applied by the adhesion per talin molecule were generally lower (Figure 4.4B,C, Figure S3).

As was done for talin, dSTORM was used to relate the abundance of vinculin, paxillin, and FAK to force applied by a cell matrix adhesion. Similar to talin, the number of vinculin and paxillin molecules in a cell matrix adhesion positively correlated with force application on both 47.2 kPa and 11.6 kPa substrates (Figure S3). By contrast, the number of FAK molecules in an adhesion and force application were uncorrelated on both of the substrates (Figure S3). Using a linear fit, quantitative relations were determined between the number of talin, vinculin, and paxillin molecules in a cell matrix adhesion and the traction force applied by that adhesion. On a substrate with an effective Young's modulus of 47.2 kPa, for each additional talin molecule an increase in the traction force of 66 pN was determined (Figure 4.4C). Vinculin and paxillin molecules were associated with ∼50% of this force: for each additional vinculin and paxillin molecule, an increase in force of 30 pN and 32 pN was determined, respectively (Figure 4.4C). On a substrate with an effective Young's modulus of 11.6 kPa, force increments were less steep and a particularly strong decrease in force associated with vinculin was observed: 27 pN/talin, 4.9 pN/vinculin, and 10 pN/paxillin (Figure 4.4C).

Together these findings indicate that i) talin, vinculin, and paxillin recruitment to cell matrix adhesions is associated with distinct increments in force; ii) on a substrate of ∼50 kPa an increase in local traction force of ∼60 pN is accompanied by recruitment of 1:2:2 talin:vinculin:paxillin molecules; iii) on a ∼4 times softer substrate force increments per molecule are less pronounced and vinculin-related force decreases dramatically; iv) FAK recruitment is not significantly associ-

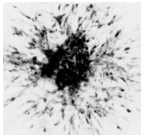

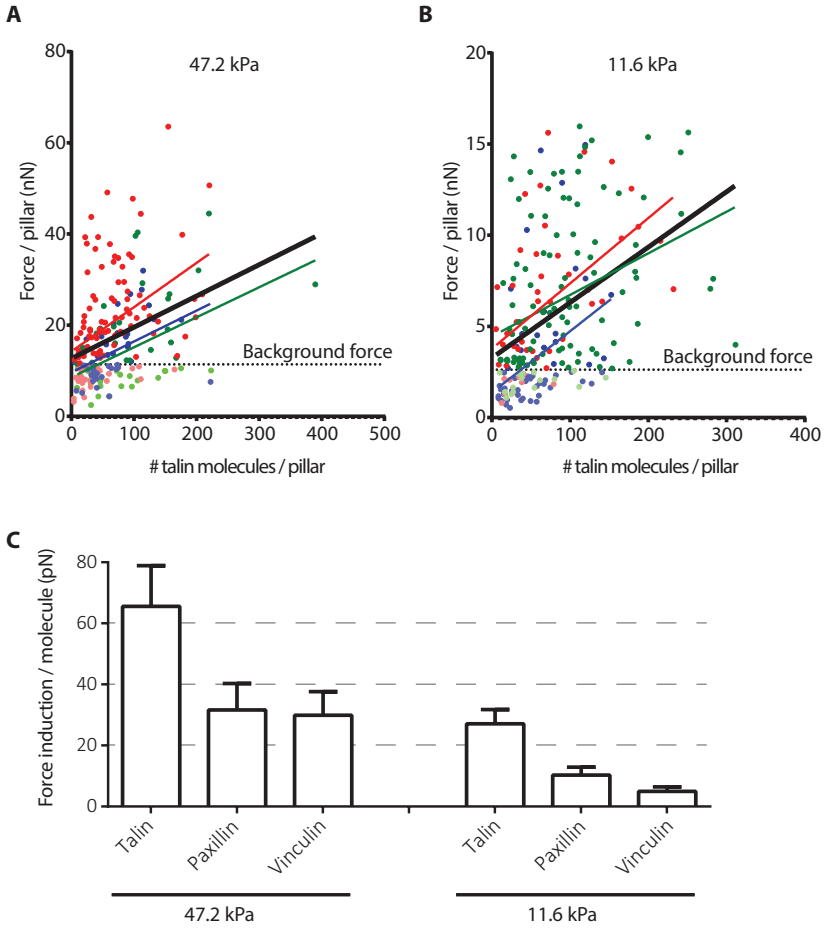

Figure 4.4

Recruitment of talin, vinculin, and paxillin to cell matrix adhesions is associated with distinct increments in force that depend on substrate stiffness. *A, B, measured force per cell matrix adhesion plotted against calculated number of talin molecules per adhesion for cells seeded on substrates with effective Young's modulus 47.2 kPa (A) and 11.6 kPa (B). Dots indicate individual adhesions; lines indicate linear fits. Red, green and blue colors represent data from three independent experiments. Solid black line represents linear fit for all data points from all three experiments. Dashed horizontal black line denotes the background forces measured. C, bar graphs showing linear fit slope values for relation between local traction force and number of talin, paxillin and vinculin molecules for cells seeded on substrates with effective Young's modulus 47.2 kPa and 11.6 kPa.*

ated with the amount of local traction force.

4.3 Discussion

Cell matrix adhesions are highly dynamic multiprotein complexes that allow cells to sense and respond to physical cues from their surrounding ECM. We combined micropillar based traction force microscopy with super resolution microscopy to obtain quantitative relationships between cell matrix adhesion composition and local traction force. In order to obtain the molecular composition from dSTORM data we developed a novel mathematical method that makes use of the high localization precision inherent in super resolution methods. We find distinct force relationships for talin, vinculin, and paxillin that are modulated by environmental stiffness, whereas recruitment of FAK molecules is not related to the amount of local traction force (Figure 4.5).

Similar to previous findings [10–12], we observe that larger adhesions support higher traction forces. Importantly, the increase in force associated with an additional talin, vinculin, or paxillin molecule does not represent the force exerted on these molecules but the overall force on the adhesion. Several additional cell matrix adhesion proteins (that are not analyzed in our current study) are likely to be recruited to the growing adhesion as it applies more traction force. These include proteins that couple integrins to the cytoskeleton, such as α-actinin and filamin [16] and their contribution has not been addressed here. As a single talin molecule interacts with a single integrin molecule, our finding that 1 additional talin molecule is associated with an additional 60 pN traction force on a ∼50 kPa substrate may point to an additional integrin being recruited to the adhesion with this increase in force. Alternatively, integrins may switch from interaction with filamins or α-actinin to interaction with additional recruited talin molecules under increased force.

It has been reported that FAK is necessary for cellular traction force generation [17] and blocking myosin II activity impairs FAK recruitment to cell matrix adhesions [18]. In that study myosin activity was blocked with blebbistatin (20 µM) resulting in very small adhesions (0.17 μm^2). We show that FAK recruitment to cell matrix adhesions does not correlate with increased traction forces on short or long pillars. This does not imply that FAK is not implicated in force generation. It has been shown that FAK activation through phosphorylation is force dependent

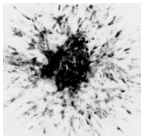

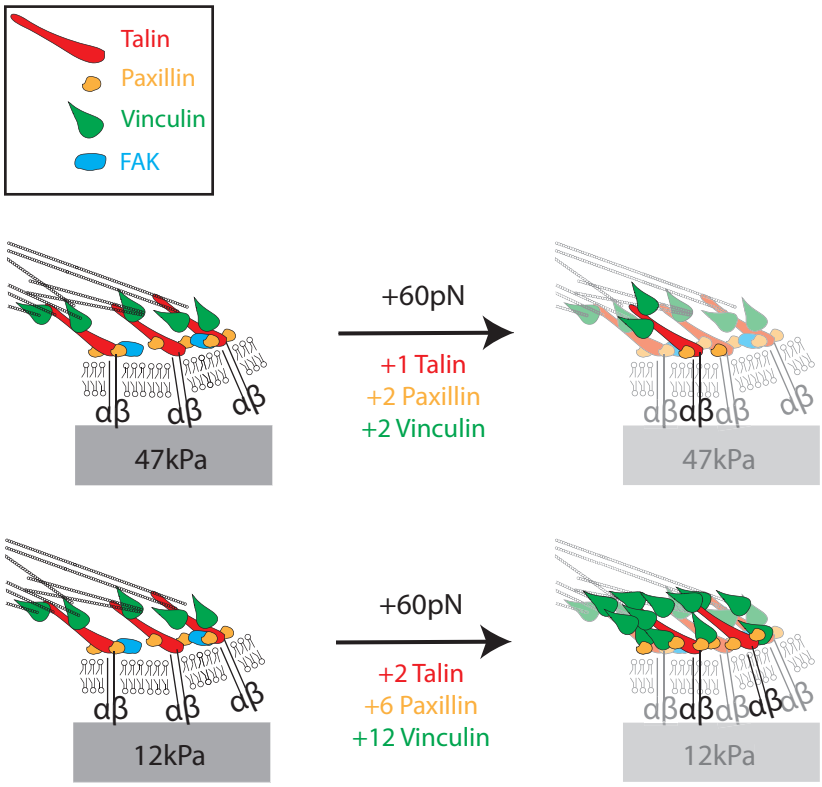

Figure 4.5
Molecular composition of force responsive cell matrix adhesions. *Cartoons depicting recruitment of talin, paxillin and vinculin molecules associated with a ∼60 pN increase in force on stiff and soft substrates with indicated effective Young's moduli.*

[19] and, in turn influences force dependent phosphorylation of paxillin and recruitment of vinculin [18]. Our findings, together with studies showing that FAK residence times are low and increase with increasing cell matrix adhesion size [18, 20] suggest that changes in FAK activity rather than its recruitment are coupled to force.

We find that the abundance of talin molecules is associated with the highest traction forces in cell matrix adhesions on stiff as well as softer substrates as compared to vinculin and paxillin. On a stiff substrate an increase in traction force of ∼60 pN is associated with one additional talin molecule, whereas two additional vinculin or paxillin molecules are associated with the same force increase (Figure 4.5). Talin connects the integrin to actin and acts as a scaffold for vinculin binding [21]. Binding of talin to the integrin cytoplasmic tail activates the integrin and enhances ECM binding, and interaction of talin with integrin αvβ3 is important for adhesion strengthening [22]. Forces on talin molecules open cryptic binding sites for vinculin [23]. It has been shown that induction of myosin contractility triggers this unfolding, which is also correlated with more actin proximal localization of vinculin and adhesion maturation [8]. This suggests that recruitment of talin and vinculin as well as their interaction is important for force related adhesion maturation. As described above, vinculin can also be recruited to cell matrix adhesions through FAK-mediated phosphorylation of paxillin, a process that depends on myosin-mediated contractility [8, 18].

Experiments with isolated talin molecules have shown that cryptic vinculin binding sites become available when talin is under 5-25 pN tension [24]. The 66 pN or 27 pN increase in traction force measured for a cell matrix adhesion on a stiff or soft substrate, respectively, per additional talin molecule is above the threshold for opening vinculin binding sites and below the 100 pN forces that can be supported by single actin molecules [25]. Notably, vinculin molecules that are recruited to the adhesion via talin, phospho-paxillin or other interactions such as force dependent p130Cas-vinculin binding [26], may partially remain in an inactive confirmation, especially on a soft substrate, which may explain the lower force induction measured for each recruited vinculin molecule as compared to talin.

Interestingly, it has been reported that as adhesions enlarge, forces on individual vinculin molecules decrease [27]. A recent publication shed more light on this by demonstrating a switch behavior for vinculin: for

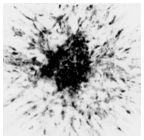

very small and very large adhesions tension on vinculin molecules negatively correlated with adhesion growth while for adhesions of intermediate size, a positive correlation of vinculin tension with adhesion growth was found [28]. The fact that vinculin has comparatively slow turnover in cell matrix adhesions on glass and that inhibition of myosin contractility raises its turnover to that observed for other cell matrix adhesion proteins further suggests that vinculin changes function with force [18, 29]. Our findings extend these observations showing that a decrease in substrate rigidity leads to a major decrease in vinculin-associated force on softer substrates: i.e. for the same amount of force increase many more vinculin molecules are recruited on a soft versus a stiff substrate (Figure 4.5). Vinculin activation is proposed to occur through its interaction with talin [8]. Larger forces applied on stiff substrates in our experiments may enhance talin-vinculin interaction, thereby more effectively supporting vinculin activation and subsequent coupling of vinculin to the actin cytoskeleton.

Taken together, we have combined dSTORM and traction force microscopy to obtain quantitative information on the relationship between the molecular composition of cell matrix adhesions and their force application. We report that an increase in force of ∼60 pN is accompanied by recruitment of 1:2:2 talin:vinculin:paxillin molecules on a substrate of ∼50 kPa (Figure 4.5). This stoichiometry changes on softer substrates, in particular due to a strong reduction of vinculin-associated force. Our novel mathematical method for extraction of molecular information from super resolution images is readily applicable to other cellular structures given that there is enough signal amplification, i.e. there are multiple fluorophores attached to the protein of interest and/or multiple blinking events observed per fluorophore.

4.4 Materials and methods

4.4.1 Cell culture and transduction

Vinculin KO MEFs (kindly provided by Dr. Johan de Rooij, Utrecht University, NL) and NIH-3T3 fibroblasts were cultured in medium (DMEM; Dulbecco's modified Eagle's Medium, Invitrogen/Fisher Scientific) supplemented with 10% new born calf serum, 25 U/ml penicillin and 25 µg/ml streptomycin (Invitrogen/Fisher Scientific cat. # 15070-063).

Vinculin KO MEFs were transduced with a GFP-vinculin retroviral construct as previously described [30].

4.4.2 Micropillar preparation and cell seeding

Micropillars were used for cellular traction force measurements according to methodology described previously [11]. A negative silicon master was made with 10x10 mm arrays of circular holes of 4.1 or 6.9 µm depth, 2 µm diameter and 4 µm center-to-center distance in a hexagonal grid with two rectangular spacers of 10x2 mm aligned on the sides of the arrays using a two-step Deep Reactive Ion Etching (DRIE) process. Negative silicon master was passivated with trichloro silane (Sigma Aldrich) and well-mixed PDMS at 1:10 ratio (crosslinker:prepolymer) was poured over the wafer and cured for 20 hours at 110°C. Pillar arrays of 4.1 and 6.9 µm height had a bending stiffness of 66 nN/µm and 16 nN/µm respectively corresponding to an effective Young's modulus, E_{eff}, of 47.2 and 11.6 kPa respectively [15]. Stamping of fibronectin was performed using a flat piece of PDMS (1:30 ratio, cured 16 hours at 65°C) previously incubated with 40 µL mix of 50 µg/mL unlabeled fibronectin (Sigma Aldrich) and 10 µg/mL Alexa405 or Alexa647 (both from Invitrogen)-conjugated fibronectin. Subsequently the micropillars were blocked with 0.2% Pluronic (F-127, Sigma Aldrich) and cells were seeded in single cell density in complete medium and incubated for 5 hours at 37°C and 5% CO_2.

4.4.3 Fixation and immunostaining

Samples were washed once with cytoskeleton buffer (CB) (10 mM MES, 150 mM NaCl, 5 mM EGTA, 5 mM $MgCl_2$, and 5mM glucose) [31], briefly permeabilized during fixation for 10 seconds with 0.1-0.25% Triton-X, 0.4% paraformaldehyde and 1 µg/mL phalloidin in CB. The triton concentration was adjusted per batch of CB to minimize the background signal without causing additional reduction to the force application. Samples were finally fixed for 10' with 4% formaldehyde in CB, permeabilized for 10' with 0.5% Triton-X and blocked for 30' with 0.5% BSA in PBS. Immunostaining was performed either with an Alexa-532-conjugated GFP nanobody (Chromotek, Germany) or with a primary mouse monoclonal antibody against talin (Sigma, T-3287), FAK (BD Transduction, 610087), paxillin (BD Transduction, 610052) or vinculin

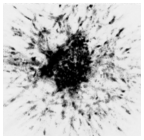

(Sigma, V-9131), followed by an Alexa647 conjugated secondary antibody against mouse IgG (Jackson, 115-605-006) following the protocol suggested by [13].

4.4.4 Imaging and analysis

dSTORM imaging

Super-resolution imaging was performed on a home-built wide-field single-molecule setup, based on an Axiovert S100 (Zeiss) inverted microscope equipped with a 100x 1.4NA oil-immersion objective (Zeiss, Germany). Micropillar arrays were inverted onto #0, 25 mm diameter, round coverslips (Menzel Glaser). Imaging was performed in 100 mM mercaptoethylamine (MEA, Sigma Aldrich) in PBS. A 405 nm laser (CrystaLaser, USA) was used for imaging the pillars and photoswitching of the Alexa647 dye to adjust the density of visible fluorophores. The light was reflected into the objective by a dichroic mirror (ZT405/532/635rpc, Chroma, USA). The fluorescence light in the detection path was filtered using the emission filter ZET532/633m (Chroma, USA). Conversion intensities were between 0 and 250 W/cm^2 at 405 nm, and the excitation intensity was 5 kW/cm^2 at 647 nm. For each sample, we acquired 20000 images with an acquisition time of 10 ms per frame and a frame rate of 69 Hz. The signal of individual dye molecules was captured on a sCMOS Orca Flash 4.0V2 camera (Hamamatsu, Japan). The average integrated signal of a single dye molecule was 608 detected photons, spatially distributed by the 2 dimensional point-spread-function of the microscope of 440 nm FWHM, resulting in a sigma of 187 nm in a Gaussian approximation.

The signal from individual fluorophores was fitted with a 2-dimensional Gaussian using a custom least-squares algorithm in Matlab [32]. From the fit we determined the location of each fluorophore to an accuracy of 14±5 nm on average (Figure 4.3B). The localization accuracy is above the theoretical minimum predicted from the width of the point-spread-function and the detected signal, $187nm/\sqrt{520} = 8.2$ nm.

Obtaining and fitting the cumulative distribution function

From the position data of the adhesion, the two-point spatial correlation function g(r) and subsequently the cumulative distance function (cdf) could be calculated as

$$cdf(r) = \int_0^r g(r')dr'.$$

For discrete 2D position data $r_i=x_i,y_i$, as obtained in super-resolution microscopy, the cdf was constructed from

$$cdf(r) = 2\sum_{i=1}^{N}\sum_{j=i+1}^{N}(x_i - x_j)^2 + (y_i - y_j)^2 < r^2.$$

The cdf describes the number of distances that are smaller than r, in a sample of N localizations. We assumed a Gaussian distribution in space leading to a cdf,

$$\mathrm{cdf(r)}=N_c(1\text{-}e^{-r^2/4\sigma^2}),$$

as the correlation length, σ_i, is given by a combination of the localization uncertainty for an individual fluorophore, Δr_i, and the size of a primary and secondary antibody complex used to label the protein of interest and typically, both detection and labeling originate from statistical processes. Here N_c is the total number of correlated distances and σ the mean positional uncertainty for all localizations. This equation is valid for $r\sim\sigma$. On length scales longer than the correlation length the cdf was characterized by a distance distribution for uncorrelated molecules. Assuming a homogeneous, random organization of molecules within a given field-of-view of area, A, the cdf of uncorrelated localizations gave a quadratic dependence on distance as:

$$\mathrm{cdf(r)}=N_u(\pi r^2)/A,$$

where N_u is the number of uncorrelated distances. Thus, the general form for the spatial correlation function was a linear combination of the correlated and the uncorrelated part:

$$\mathrm{cdf(r)}=N_c(1\text{-}e^{-r^2/4\sigma^2})+N_u(\pi r^2)/A.$$

Running a simulation with 2048 individual molecules randomly positioned in a box of 2×2 µm^2 and each molecule reappearing 100 times with a positional accuracy of 20 nm (Figure S1D) the distance distribution was calculated and its dependence on the squared distance, r^2, is shown (Figure S1E). For squared distances beyond 4×10^{-3} µm^2 the cdf(r) became linearly dependent on r^2 with the slope of $\pi N_u/A$ and y-intersect at $N_c(2\times10^7)$ as predicted.

Calculation of number of molecules from the fit

From N_c the number of molecules was calculated as following. The number of localizations, N, originating from N_m molecules each being observed n_i times is given by

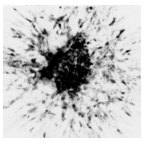

$$N = \sum_{i=1}^{N_m} n_i = N_m < n >,$$

where <n> is the average number of observations per molecule. Hence

$$N^2 = (N_m < n >)^2.$$

Likewise, the total number of correlated distances, N_c per molecule is given by $n_i \times (n_i\text{-}1)$. For all molecules this yields:

$$N_c = \sum_{i=1}^{N_m} (n_i^2 - n_i) = (N_m) < n^2 > -N.$$

Therefore

$$N^2/(N_c + N) = (N_m < n >)^2/((N_m) < n^2 >).$$

Rearranging these equations gives

$$N_m = N^2/(N_c + N)(1 + (var(n))/ < n >^2),$$

where $var(n) =< n^2 > - < n >^2$, is the variance in the number of detections per molecule. The second term, $(1 + (var(n))/ < n >^2)$, summarizes the properties of the joined statistics of labeling and photophysics of the fluorophores and its value varies between 1 and 2 depending on which of the various processes dominates the joined statistics and for a typical dSTORM experiment is close to one (see the Supplemental materials for a more detailed analysis). Simulations were performed for densities between 40 and 4000 randomly distributed molecules on an area of 2×2 µm^2. One hundred localizations per molecule were simulated with a mean positional accuracy σ = 20 nm. At high densities there was significant overlap of molecules within the image (Figure S1D). The number of estimated molecules faithfully followed the input within an accuracy of 10% (Figure S1F)

Estimation of number of molecules in an adhesion

In the quantification of the number of correlated distances it was assumed that all molecules were randomly organized, which is not the case for molecule clusters that are observed in a cell-matrix adhesion. This restriction is readily lifted by the addition of a second exponential term with weight, N_L that accounts for a length scale, L that characterizes any spatial structures in real data. Hence the cdf for a nonlinear regime becomes

$$cdf(r) = N_c(1 - e^{-r^2/4\sigma^2}) + N_L(1 - e^{-r^2/L^2}).$$

For the distinction of the two components, the typical structural length scale should be significantly larger than the positional accuracy, L $> 4\sigma$, typically 40 nm for a positional accuracy of 10 nm and holds true for many cellular structures, like large membrane compartments, adhesion clusters, chromosome territories. Hence the method described above provides a very general solution for molecule counting in super-resolution microscopy where

$$N_m = N^2/(N_c + N) \times (1 + (var(n))/ < n >^2).$$

Deflection analysis

Pillar deflections were determined with approximately 50 nm precision using a specifically designed Matlab script. The pillar locations were determined from the labeled fibronectin fluorescence image using a fit to the cross-correlation function between a perfect binary circle and the local fluorescence of one pillar. Those positions were compared to those of a perfect hexagonal grid used as reference. From an undeflected array image the accuracy was found to be 47.1 nm (Figure S1B,C), this corresponds to a force accuracy of 780 pN and 3.1 nN on the pillar array of E_{eff} = 11.6 kPa and 47.2 kPa, respectively. Masks for adhesions corresponding to individual pillars of interest were manually drawn for each case.

4.4.5 Statistic analysis

p-values were calculated using F-test for linear regression analysis using GraphPad Prism 6.0.

4.5 Acknowledgements

We thank Dr. Johan de Rooij (Utrecht University, NL) for kindly providing cells and Dr. Hedde van Hoorn (VU University, NL) for his assistance with pillar deflection analysis. Financial support for this work came from the Netherlands Organization for Scientific Research (FOM 09MMC03).

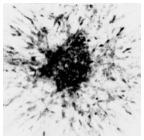

4.6 Supplemental materials

4.6.1 Obtaining the cdf

For N localizations, the total number of distances between localizations is given by N^2-N. For a typical dSTORM experiment with 10^6 localizations this would mean 10^{12} distances. If stored as double precision values this would require 8TB of memory, well beyond the limits of modern day PC's. Therefore our algorithm only takes distances into account that are smaller than a set value r_{max}. When 10^6 distances are found it terminates.

4.6.2 Relation between variance and squared mean

The factor 1+(var(n))/<n>^{2} in the equation giving the number of molecules, characterizes the joined statistics of the photophysics of the fluorophore and the statistics of labeling of the primary antibody by the secondary antibodies.

$$F = 1 + (var(n))/ < n >^2 = 1 + c_v^2$$

It is related to the coefficient of variation c_v of n = σ_n/<n> in statistics. Values for F vary between 1 and 2 depending on the underlying and dominant statistics.

Distribution	Mean	Variance	F
Binomial	n p	n p (1-p)	1 + 1/np - 1/n
Poissonian	λ	λ	1+1/λ
Exponential	1/λ	1/λ^2	2
Gaussian	μ	σ^2	1+σ^2/μ^2

4.6.3 Simulation for a combined statistics with secondary antibody labeling

A typical dSTORM experiment involves a dual labeling step where the molecule of interest is first labeled by a specific primary antibody that is subsequently labeled by multiple secondary antibodies, each conjugated to multiple fluorophores. To assess the distribution in this experiment we performed simulations. In those simulations we assumed:

1) The number of secondary antibodies bound to a primary antibody is constant, given that the excess of secondary antibody occupies all binding sites on the primary antibody.

2) The number of fluorophores bound to a secondary antibody has a Poissonian distribution with a mean of 4.7 (typical mean value provided by the manufacturer, Jackson Immunology).

3) The number of detections per fluorophore follows a single-exponential distribution, typical for photobleaching. The number of detections when a fluorophore is in the on-state equals $t_{on} \times$framerate. Alexa647, as used in the current study is generally assumed to behave according to a four-state molecule characterized by a ground, a fluorescent excited, a non-fluorescent triplet and a long-lived dark state. The latter populated via the excited triplet state [33]. The distribution in such a case is described in terms of a static trap model [34], with on-times following a single exponential distribution.

Figure S4 summarizes the result of this simulation. The factor $F=1+(\mathrm{var}(n))/\langle n\rangle^2$, is dominated by the number of secondary antibodies. For typical values found in literature as the secondary to primary ratio (4), F is found to be below 1.1. Even in the case of only a single secondary per primary F equals 1.5, which is still below its maximal value of 2. This is caused by the multiple fluorophores per secondary antibody.

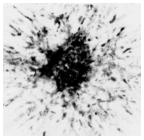

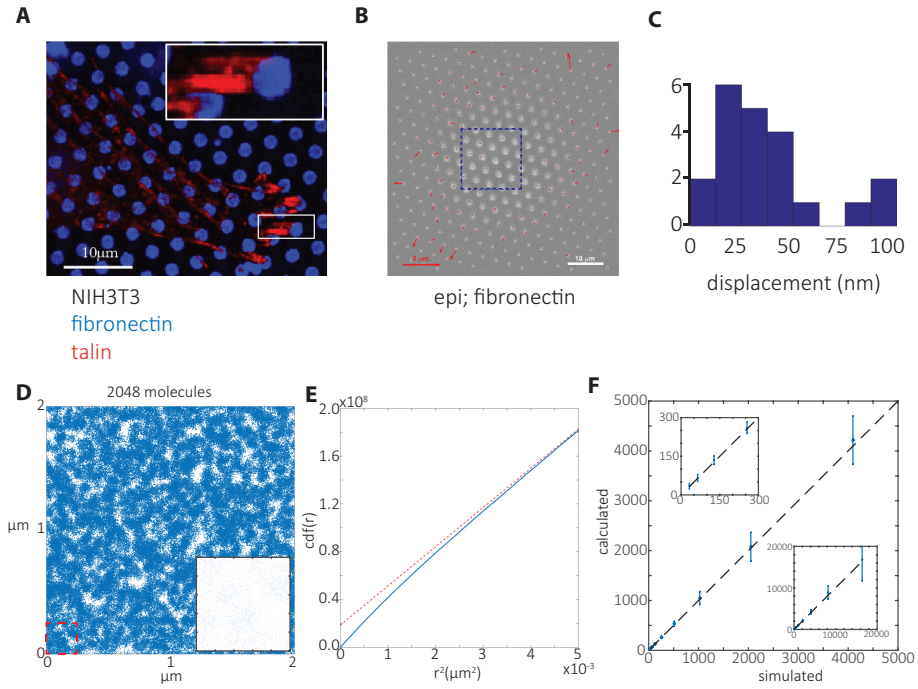

Figure S1

Pillar localization precision and analyses on simulations of molecules. *A, confocal image of a NIH3T3 cell on fibronectin (conjugated with Alexa 405) stamped PDMS pillars immunostained for talin (secondary antibody Alexa647). B, epi-fluorescence image of cell-free (force-free) PDMS pillar array obtained from dSTORM microscope with calculated pillar deflections (1024x1024 pixels). Blue box indicates area in which dSTORM measurements were performed (256x256 pixels). C, the histogram of pillar deflections measured in the boxed area (B) indicating the localization precision of pillar centers. D,E, detections from a simulation of random placement of 2048 molecules in a region of 4 µm^2 with 100 localizations per molecule (N=2048x100) with a positional accuracy of 20 nm (D), and cumulative distance function (cdf) of the inter-localization distances with a linear fit (red dashed line) with y-intercept at N_c=2x10^7, resulting in calculated N_m=N^2/(N+N_c)=2076 (E). F, calculated number of molecules N_m with standard deviation plotted against simulated number of molecules and dashed line of slope 1 with insets showing same graph with different zoom areas. Scale bars are 10 µm (A, B); deflection arrow scales are 2 µm (B).*

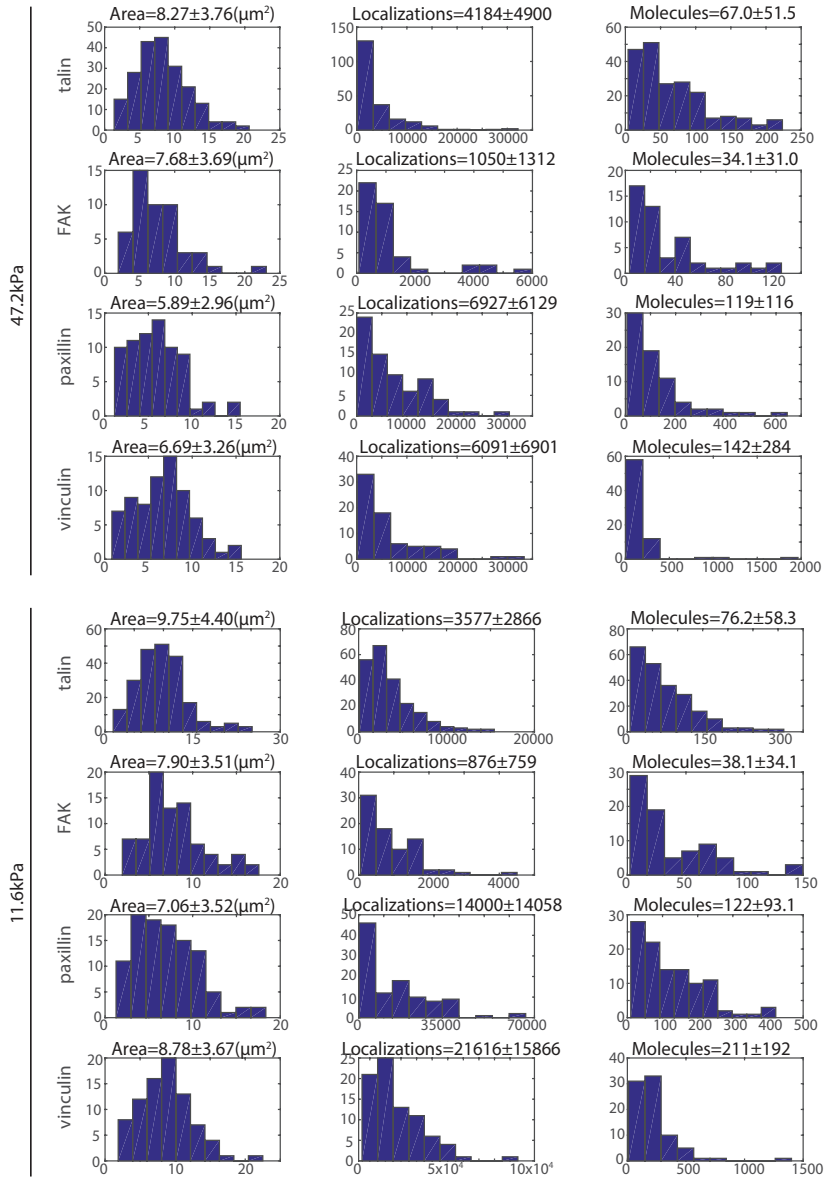

Figure S2

Histograms of adhesion area, localizations detected and molecules calculated per adhesion. *Histograms of areas of manually selected cell-matrix adhesions associated with pillars showing distribution of total cell matrix adhesion area (first column), detected localizations (second column), and calculated number of molecules (third column). Top four rows show data for adhesions coupled to pillars with effective Young's modulus of 47.2 kPa. Bottom four rows show data for adhesions coupled to pillars with effective Young's modulus of 11.6 kPa. Data for dSTORM experiments on talin (1^{st} and 5^{th} rows), FAK (2^{nd} and 6^{th} rows), paxillin (3^{rd} and 7^{th} rows) and vinculin (4^{th} and 8^{th} rows) are shown. Means and standard deviations are given above each histogram.*

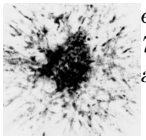

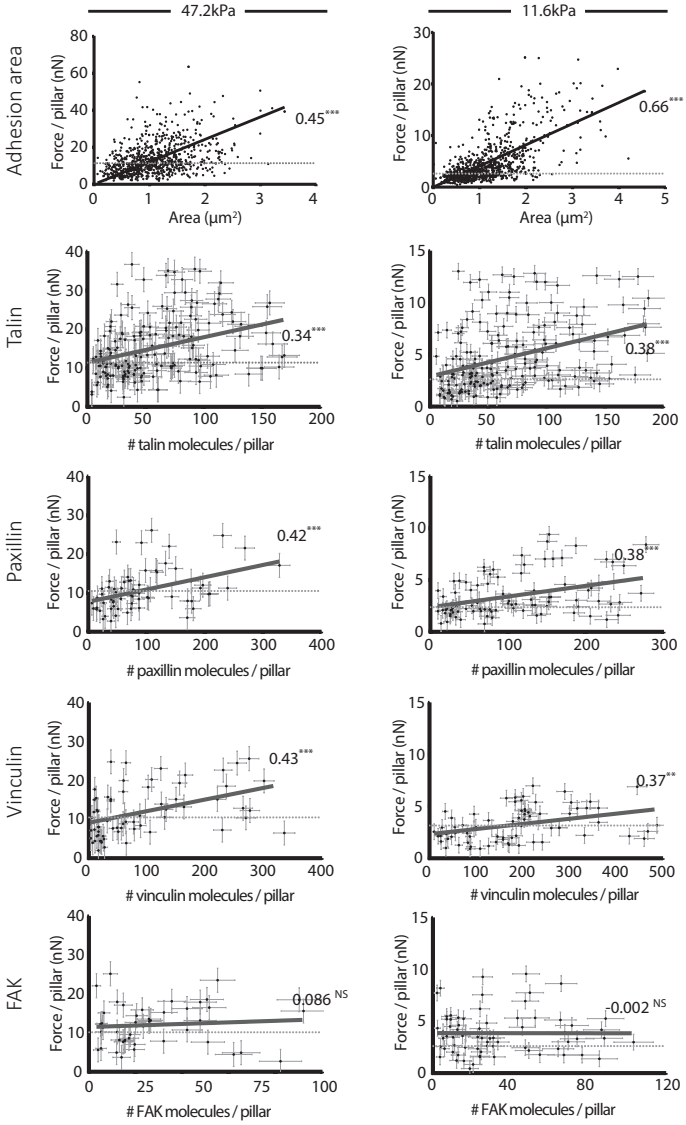

Figure S3

Total adhesion area and number of talin, vinculin, and paxillin molecules but not of FAK molecules correlates with local traction force. *Force per adhesion measured plotted against adhesion area and number of calculated talin, paxillin, vinculin and FAK molecules associated with the adhesion from three different experiments plotted with standard deviations; black solid line is the accompanying linear fit denoted with the calculated Pearson's correlation and dashed line is the measured background deflections for cells seeded on substrates with effective Young's modulus 47.2 kPa (left) and 11.6 kPa (right). ***, $p<0.0001$; **, $p<0.005$; NS: $p>0.05$: p values denote how significantly the slope is different from zero as calculated with F-test.*

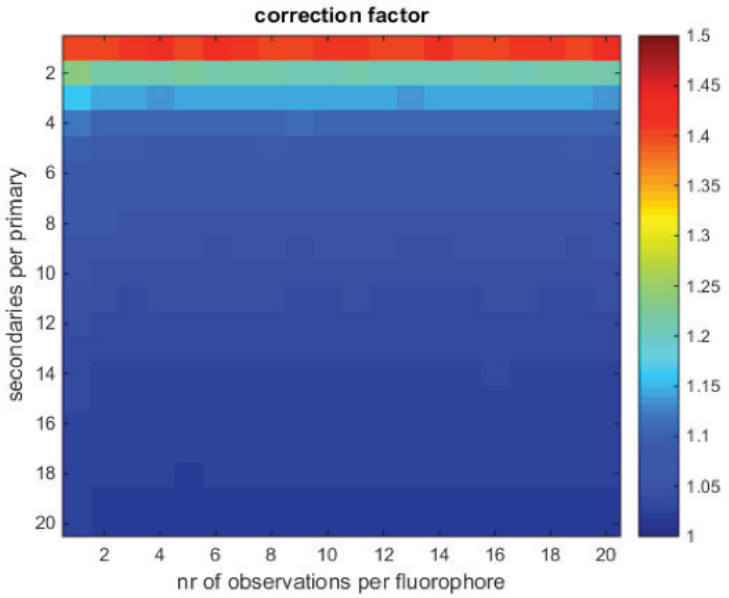

Figure S4

Simulations on correction factor, F. *Correction factor F as described in formula $F=1+var(n)/<n>^2$ for several simulations where the number of observations per fluorophore and the number of secondary antibodies per primary antibody were varied. The number of secondary antibodies per primary dominates the factor F.*

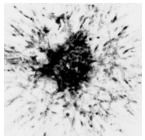

Bibliography

[1] Ekaterina Papusheva and Carl-Philipp Heisenberg. "Spatial organization of adhesion: force-dependent regulation and function in tissue morphogenesis". In: *The EMBO Journal* 29.16 (2010).

[2] Amnon Buxboim, Irena L Ivanovska, and Dennis E Discher. "Matrix elasticity, cytoskeletal forces and physics of the nucleus: how deeply do cells 'feel' outside and in?" In: *Journal of Cell Science* 123.3 (2010).

[3] Sanjay Kumar and Valerie M Weaver. "Mechanics, malignancy, and metastasis: The force journey of a tumor cell". In: *Cancer and Metastasis Reviews* 28.1-2 (2009).

[4] Simon W Moore, Pere Roca-Cusachs, and Michael P Sheetz. "Stretchy proteins on stretchy substrates: the important elements of integrin-mediated rigidity sensing." In: *Developmental Cell* 19.2 (2010).

[5] Cord Brakebusch and Reinhard Fässler. "The integrin-actin connection, an eternal love affair". In: *The EMBO Journal* 22.10 (2003).

[6] Stephan Huveneers and Erik HJ Danen. "Adhesion signaling – crosstalk between integrins, Src and Rho". In: *Journal of Cell Science* 122.8 (2009).

[7] J Thomas Parsons, Alan R Horwitz, and Martin A Schwartz. "Cell adhesion: integrating cytoskeletal dynamics and cellular tension." In: *Nature Reviews. Molecular Cell Biology* 11.9 (2010).

[8] Lindsay B Case et al. "Molecular mechanism of vinculin activation and nanoscale spatial organization in focal adhesions." In: *Nature Cell Biology* 17.7 (2015).

[9] Pakorn Kanchanawong et al. "Nanoscale architecture of integrin-based cell adhesions." In: *Nature* 468.7323 (2010).

[10] Nathalie Q Balaban et al. “Force and focal adhesion assembly: a close relationship studied using elastic micropatterned substrates”. In: *Nature Cell Biology* 3.5 (2001).

[11] Hedde van Hoorn et al. “The Nanoscale Architecture of Force-Bearing Focal Adhesions”. In: *Nano Letters* 14.8 (2014).

[12] Léa Trichet et al. “Evidence of a large-scale mechanosensing mechanism for cellular adaptation to substrate stiffness”. In: *Proceedings of the National Academy of Sciences of the United States of America* 109.18 (2012).

[13] Sebastian van de Linde et al. “Direct stochastic optical reconstruction microscopy with standard fluorescent probes”. In: *Nature Protocols* 6.7 (2011).

[14] Robert P Nieuwenhuizen et al. “Quantitative localization microscopy: effects of photophysics and labeling stoichiometry.” In: *PLoS One* 10.5 (2015).

[15] Hayri E Balcıoğlu et al. “The integrin expression profile modulates orientation and dynamics of force transmission at cell-matrix adhesions.” In: *Journal of Cell Science* 128.7 (2015).

[16] Alex-Xianghua X Zhou, John H Hartwig, and Levent M Akyürek. “Filamins in cell signaling, transcription and organ development.” In: *Trends in Cell Biology* 20.2 (2010).

[17] Ben Fabry et al. “Focal Adhesion Kinase Stabilizes the Cytoskeleton”. In: *Biophysical Journal* 101.9 (2011).

[18] Ana M Pasapera et al. “Myosin II activity regulates vinculin recruitment to focal adhesions through FAK-mediated paxillin phosphorylation.” In: *The Journal of Cell Biology* 188.6 (2010).

[19] Jihye Seong et al. “Distinct biophysical mechanisms of focal adhesion kinase mechanoactivation by different extracellular matrix proteins.” In: *Proceedings of the National Academy of Sciences of the United States of America* 110.48 (2013).

[20] Sylvia E Le Dévédec et al. “The residence time of focal adhesion kinase (FAK) and paxillin at focal adhesions in renal epithelial cells is determined by adhesion size, strength and life cycle status.” In: *Journal of Cell Science* 125.Pt 19 (2012).

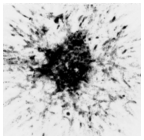

[21] Seiji Tadokoro et al. “Talin binding to integrin beta tails: a final common step in integrin activation.” In: *Science (New York, N.Y.)* 302.5642 (2003).

[22] Pere Roca-Cusachs et al. “Clustering of alpha(5)beta(1) integrins determines adhesion strength whereas alpha(v)beta(3) and talin enable mechanotransduction.” In: *Proceedings of the National Academy of Sciences of the United States of America* 106.38 (2009).

[23] Armando del Rio et al. “Stretching Single Talin Rod Molecules Activates Vinculin Binding”. In: *Science (New York, N.Y.)* 323.5914 (2009).

[24] Mingxi Yao et al. “Mechanical activation of vinculin binding to talin locks talin in an unfolded conformation”. In: *Scientific Reports* 4 (2014).

[25] Akiyoshi Kishino and Toshio Yanagida. “Force measurements by micromanipulation of a single actin filament by glass needles”. In: *Nature* (1988).

[26] Radoslav Janoštiak et al. “CAS directly interacts with vinculin to control mechanosensing and focal adhesion dynamics”. In: *Cellular and Molecular Life Sciences* 71.4 (2013).

[27] Casten Grashoff et al. “Measuring mechanical tension across vinculin reveals regulation of focal adhesion dynamics”. In: *Nature* 466.7303 (2010).

[28] Pablo Hernández-Varas et al. “A plastic relationship between vinculin-mediated tension and adhesion complex area defines adhesion size and lifetime.” In: *Nature Communications* 6 (2015).

[29] Haguy Wolfenson et al. “Actomyosin-generated tension controls the molecular kinetics of focal adhesions”. In: *Journal of Cell Science* 124.9 (2011).

[30] Erik H J Danen et al. “Integrins control motile strategy through a Rho-cofilin pathway”. In: *The Journal of Cell Biology* 169.3 (2005).

[31] Johanna Prast, Mario Gimona, and Victor J Small. “Immunofluorescence microscopy of the cytoskeleton: combination with green fluorescent protein tags”. In: *Cell Biology: A Laboratory Handbook (3rd ed) JECelis, ed. Amsterdam* (2006).

[32] Thomas Schmidt et al. “Imaging of single molecule diffusion”. In: *Proceedings of the National Academy of Sciences of the United States of America* 93.7 (1996).

[33] Thomas Schmidt et al. “Characterization of Photophysics and Mobility of Single Molecules in a Fluid Lipid Membrane”. In: *The Journal of Physical Chemistry* 99.49 (1995).

[34] Frank Cichos, Christian von Borczyskowski, and Michel Orrit. “Power-law intermittency of single emitters”. In: *Current Opinion in Colloid & Interface Science* 12.6 (2007).